RSC Advances

PAPER

View Article Online
View Journal | View Issue



Cite this: *RSC Adv.*, 2023, **13**, 15334

# Infrared sensitive mixed phase of $V_7O_{16}$ and $V_2O_5$ thin-films†

Anchal Rana,[a] Aditya Yadav,[b] Govind Gupta [b] and Abhimanyu Rana *[a]

Received 4th February 2023
Accepted 16th May 2023

DOI: 10.1039/d3ra00752a

rsc.li/rsc-advances

We report an infrared (IR) sensitive mixed phase of $V_7O_{16}$ and $V_2O_5$ thin films, grown by cathodic vacuum arc-deposition on glass substrates at relatively low temperatures. We have found that the mixed phase of $V_7O_{16}$ and $V_2O_5$ can be stabilized by post-annealing of amorphous $V_xO_y$ between 300–400 °C, which gets fully converted into $V_2O_5$ after annealing at higher temperatures ~450 °C. The local conversion from $V_xO_y$ to $V_2O_5$ has also been demonstrated by applying different laser powers in Raman spectroscopy measurements. The optical transmission of these films increases as the content of $V_2O_5$ increases but the electrical conductivity and the optical bandgap decrease. These results are explained by the role of defects (oxygen vacancies) through the photoluminescence (PL) and time-resolved photoluminescence (TRPL) measurements. The IR sensitivity of the mixed phase is explained by the plasmonic absorption by the $V_7O_{16}$ degenerate semiconductor.



## Introduction

Infrared (IR) sensitive materials have been of significant interest for IR sensors and smart windows in which the resistance or the optical transmission can be modulated by heating or IR radiation.[1,2] Therefore, many low-bandgap semiconductors,[3,4] quantum-well heterostructures[5] and high-temperature-superconductors[6,7] are intensively studied. However, these materials need to be cooled at lower temperatures for these applications. Vanadium-based oxides, found in more than 52 stable and metastable phases, have been investigated for developing uncooled devices as they show metal–insulator transitions (MIT) close to room temperatures under different external stimuli such as thermal, electrical, and optical.[8–14] Vanadium (V) can have oxidation states varying from +2 to +5, where $V_2O_3$, $VO_2$, and $V_2O_5$ are the most studied phases but other non-stoichiometric phases such as $V_3O_7$, $V_4O_9$, $V_6O_{13}$, $V_7O_{16}$ have also been reported, that occur due to the presence of more than one valency of V atom in a single crystal structure.[14–17] Although, $VO_2$ (having $V^{4+}$ valency) has been the most preferred phase for IR sensors[10,11,18] and smart windows due to sharp MIT close to room temperature,[19–22] it has limitations of growing in the right phase on arbitrary substrates at low temperatures. On the other hand, $V_2O_5$ having a layered structure is important for energy storage electrodes,[23–26] gas sensors[27–29] and chromogenic applications.[30–32] However, the applicability of the pure $V_2O_5$ phase is again largely restricted due to high temperature growth and poor electrical conductivity. The mixed phase of $VO_2$ and $V_2O_5$ has been reported to give enhanced IR sensitivity.[33] Other phases such as $V_7O_{16}$ could be promising for these applications which has the mixture of both $V^{4+}$ and $V^{5+}$ arranged in a layered crystal structure.[15,34,35] However, there are very few reports on $V_7O_{16}$ phase which has been reported during chemical synthesis of $V_2O_5$ nanotubes[28,35] or in thin film form when grown under oxygen deficient conditions using pulsed laser deposition[29] and atomic layer deposition.[15] There is a clear research gap for in-depth understanding of electronic and optical properties of $V_7O_{16}$ for any practical application in smart windows and IR sensors. Here, we systematically tune the contents of $V_7O_{16}$ and $V_2O_5$ in a mixed phase (also changing the $V^{4+}$ and $V^{5+}$ ratio) by post-annealing of amorphous vanadium oxide thin films grown by cathodic vacuum arc-deposition. We report a strong modulation of electrical resistance and optical transmission in these films with IR radiation and temperature.

## Materials and methods

First an amorphous vanadium oxide thin films were grown on high-grade barium-borosilicate 7059 glass substrates using cathodic vacuum arc-deposition by evaporating a vanadium metal target (~99.99% purity) in the presence of oxygen at a partial pressure of $\sim 1 \times 10^{-3}$ mbar, arc current of ~150 A, substrate temperature ~200 °C and substrate bias of −60 V. These films were then taken out and annealed in air at different temperatures *i.e.*, ~300 °C, ~350 °C, ~400 °C, ~450 °C, and 520 °C for 2 hours. The unannealed sample will be called as $S_{as\text{-}grown}$ and other annealed sampled as $S_{300}$, $S_{350}$, $S_{400}$, $S_{450}$, and

[a]*Centre for Advanced Materials and Devices, School of Engineering and Technology, BML Munjal University, Sidhrawali, Gurugram-122413, Haryana, India. E-mail: rana.abhimanyu@gmail.com*

[b]*CSIR-National Physical Laboratory, K. S. Krishnan Marg, New Delhi, 110012, India*

† Electronic supplementary information (ESI) available. See DOI: https://doi.org/10.1039/d3ra00752a

$S_{520}$ in this manuscript. The Raman spectroscopy was carried out using a commercial spectrometer by WiTech (Alpha 300) having a green laser of 532 nm wavelength. The crystal structure was confirmed by X-ray diffraction (XRD, Panalytical Empyrean Model) by scanning $2\theta$ ranging from 10° to 90° at a step size of 0.02° using Cu K$\alpha$ radiation ($\lambda \sim 1.54$ Å). The X-ray photoelectron spectroscopy (XPS) was carried out using XPS/ESCA, K-ALPHA+, Thermo Fisher Scientific. The deconvolution and fitting of XPS data of was performed using XPSpeak41 software. The optical transmission spectra were obtained in the wavelength range from 380 nm to 800 nm using a UV-visible spectrometer by PerkinElmer LAMBDA 365 model. Electrical measurements were performed using a four-probe setup equipped with Keithley electrometers. The IR sensing measurements were carried out using the IR source by Newport model 6363IR having intensity ~438 W $m^{-2}$. Photoluminescence (PL) and time-resolved photoluminescence (TRPL) were recorded at the excitation wavelength of ~350 nm and ~266 nm (pulsed) using Edinburgh (FLS 980D2D2) set-up.

## Results and discussion

The XRD patterns of $S_{as\text{-}grown}$, $S_{300}$, $S_{350}$, $S_{400}$, $S_{450}$, and $S_{520}$ are shown in Fig. 1(a) with their corresponding photographs in the inset. Apparently, the photographic images show a clear change in colour from black (of amorphous films) to the yellowish orange after annealing. There is also a clear transition in XRD spectra from a broad hump in $S_{as\text{-}grown}$ to sharp peaks in annealed samples at ~15.3°, ~20.18°, ~21.65°, ~31.04°, ~41.21° and ~41.87° related to (020), (001), (011), (040), (002), and (012) crystalline planes of the pure orthorhombic phase of $V_2O_5$ respectively. However, the peak at ~24.5° confirms the presence of the $V_7O_{16}$ triclinic phase[15,34] in $S_{350}$ and $S_{400}$ samples.

To further confirm the presence of $V_7O_{16}$, the X-ray photoelectron spectroscopy (XPS) were performed on $S_{300}$ and $S_{520}$, as shown in Fig. 1(b, c) and (d, e) respectively. The binding energy peak ~284.8 eV of carbon 1s orbital was used to compensate the shifts in other peaks due to charging. The XPS spectra for 2p orbitals of vanadium (V) has two peaks corresponding to $2p_{3/2}$ and $2p_{1/2}$ due to the spin–orbit splitting of ~7.5 eV. However, each peak $2p_{3/2}$ and $2p_{1/2}$ were further deconvoluted that correspond to the presence of $V^{4+}$ (~516.5 eV & ~524 eV) and $V^{5+}$ (~517.5 eV & ~525 eV).[15,36] The peak at ~530 eV is related to 1s oxygen in vanadium oxygen bonds,[37,38] but other peaks at higher energies ~532 eV are due to free hydroxyl groups adsorbed on the hydrophilic surfaces.[39] The ratio of $V^{4+}$ and $V^{5+}$ contents in $S_{300}$ and $S_{520}$, estimated by the dividing the area under the curve of respective peaks, is found to be consistent with literature,[15,40] implying higher $V^{4+}$ content in these samples having $V_7O_{16}$ phase. In $S_{520}$, peaks corresponding to $V^{4+}$ were observed because of the photoreduction of $V^{5+}$ in $V_2O_5$ phase.[41]

The Raman spectroscopic results of these films are compared in Fig. 2. Due to the amorphous nature of $S_{as\text{-}grown}$ film, no sharp peaks were observed but as annealing temperature exceeds 300 °C, sharp peaks start appearing. The Raman spectra for $S_{450}$ and $S_{520}$ shows peaks at ~101, ~144, ~194, ~282, ~304, ~404, ~483, ~507, ~528, ~699, and ~992 $cm^{-1}$ due to different vibrational modes of $V_2O_5$ phase,[14,15,42–44] as description given in Table 1. Especially, the strongest peak at ~144 $cm^{-1}$ arises from the V–O–V chains of the layered structure of $\alpha$-$V_2O_5$, as shown in Fig. 2(b). For the samples annealed below 400 °C ($S_{300}$ and $S_{350}$), the peaks around ~158, ~255, ~294, ~832, ~870, ~970 $cm^{-1}$ confirms the presence of $V_7O_{16}$

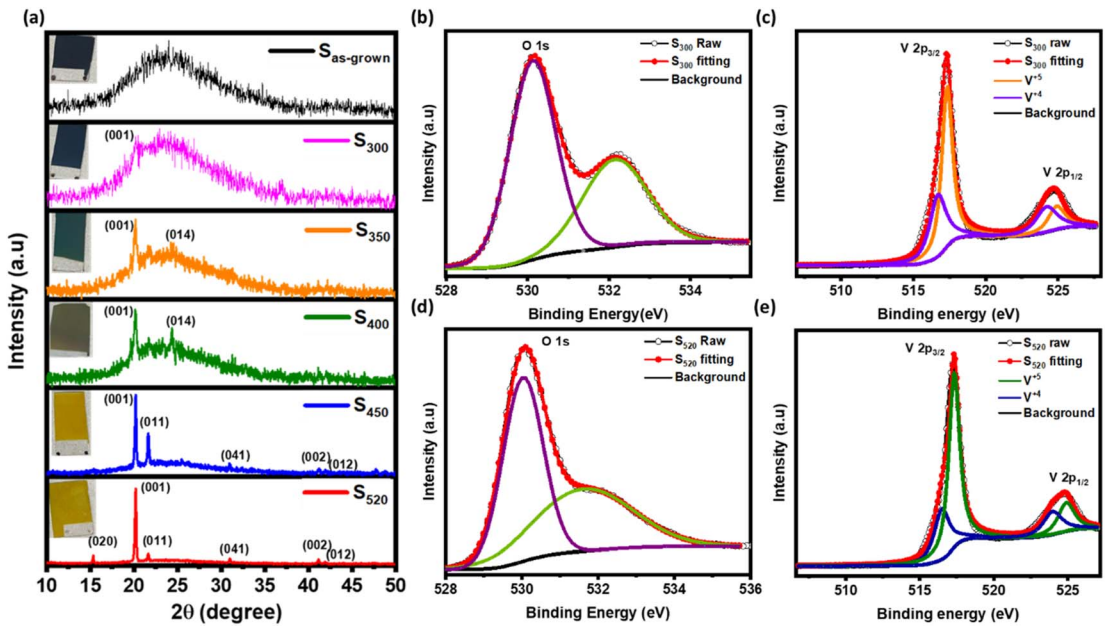


Fig. 1 (a) X-ray diffraction (XRD) spectra of vanadium oxide thin films annealed at various temperature. X-ray photoelectron spectroscopy (XPS) spectra of (b and c) $S_{300}$ and (d and e) $S_{520}$ samples shows V(2p) and O(1s) peaks.

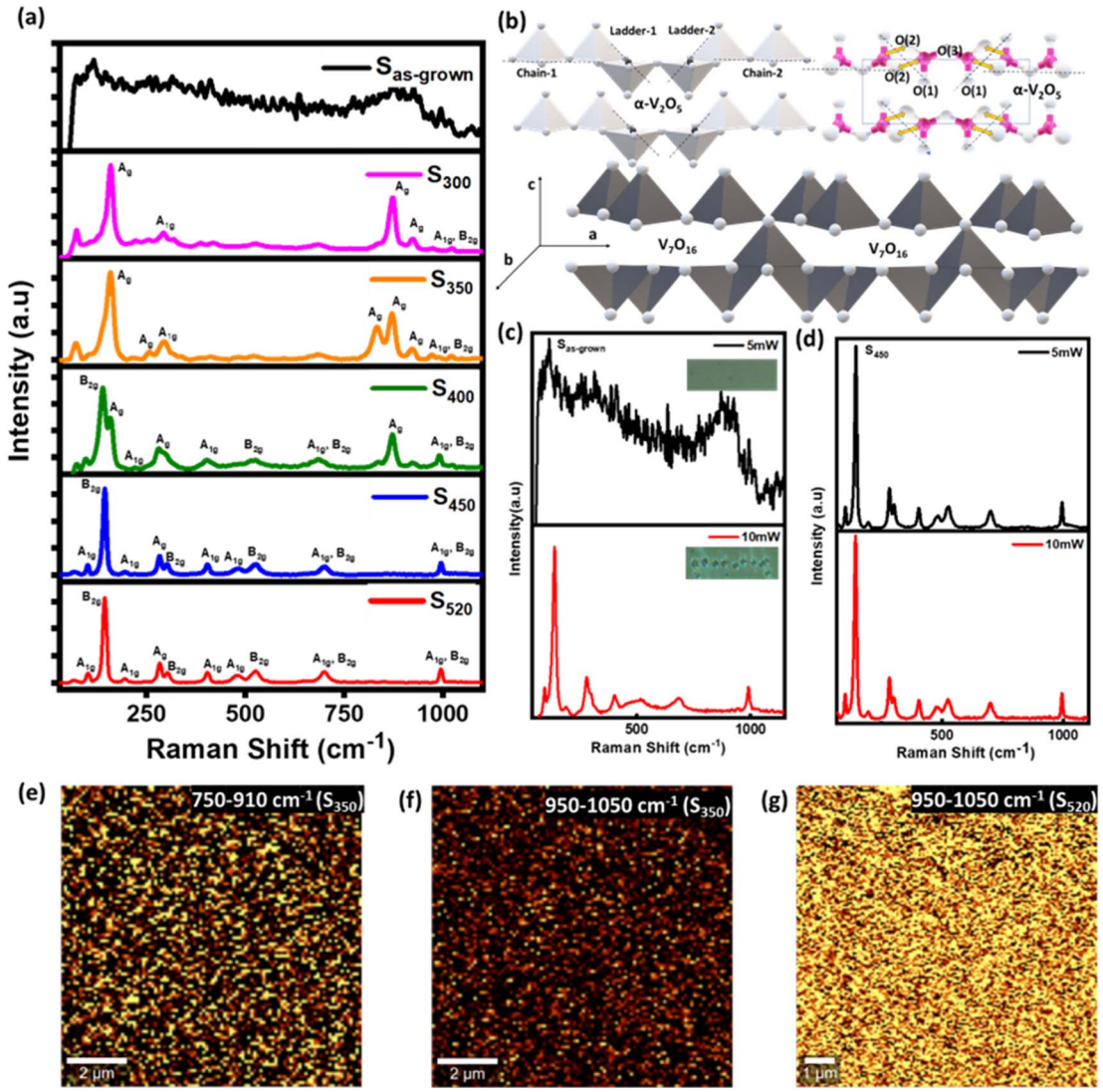


Fig. 2 (a) Raman spectra of vanadium oxide thin films annealed at various temperatures; (b) the crystal structure of α-$V_2O_5$ and $V_7O_{16}$; (c and d) $S_{as\text{-}grown}$ and $S_{450}$ samples at the laser power 5 mW and 10 mW laser power; (e–g) Raman mapping of the $S_{350}$ and $S_{520}$ samples.

phase, also consistent with the earlier studies.[14,44,45] It is to be noted that the presence of other polymorphs of $V_2O_5$ (β- γ-)[14,26,42,44] cannot be completely ruled out using Raman spectroscopy due to overlapping peak positions.[14] Fig. 2(b) shows the schematic of $V_7O_{16}$ phase where the layered structure resembles to α-$V_2O_5$, causing the peak ~144 $cm^{-1}$ to be shifted to higher wavenumber ~158 $cm^{-1}$. However, the other vibrational modes related to ladder steps (LS) seems to be missing in $V_7O_{16}$, indicating the absence of LS in this phase. Clearly, other peaks at ~255, ~294, ~832, ~870, and ~970 $cm^{-1}$ could be assigned to the vibrational modes of V=O bonds ($A_g$ symmetry).[15] Also, the Raman spectroscopy performed at different laser powers (5 mW to 10 mW) in Fig. 2(c) and (d) shows the immediate conversion of amorphous phase to $V_2O_5$, unlike the annealed samples. Similar conversion was also observed by other groups in case of chemically synthesized $VO_x$ nanotubes.[43] This study opens further questions of stabilizing the intermediate phase of $V_7O_{16}$ using laser heating and open the opportunities for applications in laser writing for high security tags and detection Fig. 2(e)–(g) shows the Raman mapping of $S_{350}$ and $S_{520}$ samples. Since the Raman spectra of the $S_{350}$ show the characteristic peaks at ~832 $cm^{-1}$, 870 $cm^{-1}$, 920 $cm^{-1}$ and $S_{520}$ at 994 $cm^{-1}$, we performed Raman mapping by selecting two wavelengths range from 750–910 $cm^{-1}$ and 950–1050 $cm^{-1}$ so that we could capture the regions of $V_7O_{16}$ and $V_2O_5$ spatially in 10 × 10 $\mu m^2$ area. In Fig. 2(e) and (f), for $S_{350}$ both $V_7O_{16}$ and $V_2O_5$ phases can be seen. On the other hand, for $S_{520}$ the brighter region mostly cover the $V_2O_5$ with some minor black regions due to some other phases.

Fig. 3(a) shows the optical transmission spectra of $S_{as\text{-}grown}$, $S_{300}$, $S_{350}$, $S_{400}$, $S_{450}$, and $S_{520}$. Apparently, the transmittance gradually increases with increasing the annealing temperature, and the maximum transmittance was observed in sample $S_{400}$. The optical band gap was calculated for all the samples by using Tauc's equations.[46] The calculated energy band gap of these samples decreases from ~2.85 eV to 2.2 eV for the samples annealed at higher temperatures [Fig. 3(c)].

Table 1 Raman-active phonon modes in mixed phase of $V_7O_{16}$ and $V_2O_5$ thin-films

| $\nu$ ($cm^{-1}$) | Description | Phonon modes |
|---|---|---|
| 101 | In phase rotation of the $V_2O_4$ ladder step (LS) unit in *b*-axis (crystalline $V_2O_5$)[14,42] | $A_{1g}$ |
| 144 | Skeleton bending of V–O–V chain (crystalline $V_2O_5$)[14] | $B_{2g}$ |
| 158 | Skeleton bending of V–O–V chain (crystalline $V_7O_{16}$)[14,15] | $A_g$ |
| 194 | Bending of O(2)–V–O(3) (crystalline $V_2O_5$)[14] | $A_{1g}$ |
| 255 | Vibration of the V=O bond (crystalline $V_7O_{16}$) | $A_g$ |
| 282 | Bending of V=O (crystalline $V_2O_5$)[14] | $A_{1g}$ |
| 294 | Bending of V=O (crystalline $V_7O_{16}$) | $A_g$ |
| 304 | Bending of V–O(2) (crystalline $V_2O_5$)[14] | $B_{2g}$ |
| 404 | Angle-bending of V–O(3)–V bonds (crystalline $V_2O_5$)[14] | $A_{1g}$ |
| 483 | Symmetric stretching of V–O(3)–V bonds (crystalline $V_2O_5$)[14] | $A_{1g}$ |
| 507 | Stretching vibrations of V–O(2) bonds (crystalline $V_2O_5$)[14] | $B_{2g}$ |
| 528 | Stretching vibrations of V–O(2) bonds (crystalline $V_2O_5$)[14] | $A_{1g}$ |
| 699 | Asymmetric stretching of V–O(2)–V bridge (crystalline $V_2O_5$) | $A_{1g}$, $B_{2g}$ |
| 832 | Stretching vibration of the V=O bond (crystalline $V_7O_{16}$)[14,15] | $A_g$ |
| 870 | Stretching vibration of the V=O bond (crystalline $V_7O_{16}$)[14,15] | $A_g$ |
| 920 | Stretching vibrations of $V^{4+}$=O bond (due to oxygen vacancies)[15] | $A_g$ |
| 992 | Stretching vibration of V=O (crystalline $V_2O_5$)[14] | $A_{1g}$, $B_{2g}$ |

Usually, the amorphous semiconductors exhibit band-tailing due to the structural disorder which can be quantified as Urbach energy ($E_u$) shown in Fig. 3(b). The amorphous $S_{as\text{-}grown}$ sample clearly having more defects shows highest $E_u$ value which decreases by increasing annealing temperature, that indicate the defects are significantly reduced after annealing. The electrical conductivity (measured by four-probe) also decreases for the samples annealed at higher temperatures, as shown in Fig. 3(d). Fig. 3(c) and (d) also shows the optical transmission integrated over the wavelength from 400–800 nm plotted on right *Y*-axis, having clear correlation with the electronic properties. The results are explained by considering a band-model shown in Fig. 3(e). Although the band gap of $V_7O_{16}$ is higher than the $V_2O_5$, it still has high conductivity due to the presence of more $V^{4+}$ content, that contribute extra electrons in 3d conduction band. Also, the amorphous and low-temperature annealed samples are expected to have large number of defects and oxygen vacancies, that can even push the Fermi level into the conduction band, making $V_7O_{16}$ a degenerate semiconductor.[23] Therefore, the overall conductivity of mixed phase is higher than the $V_2O_5$ due to the presence of $V_7O_{16}$. On the other hand, the samples annealed at high-temperature are defects free, despite having a lower bandgap and the Fermi level lies in the band gap. The dynamic resistance

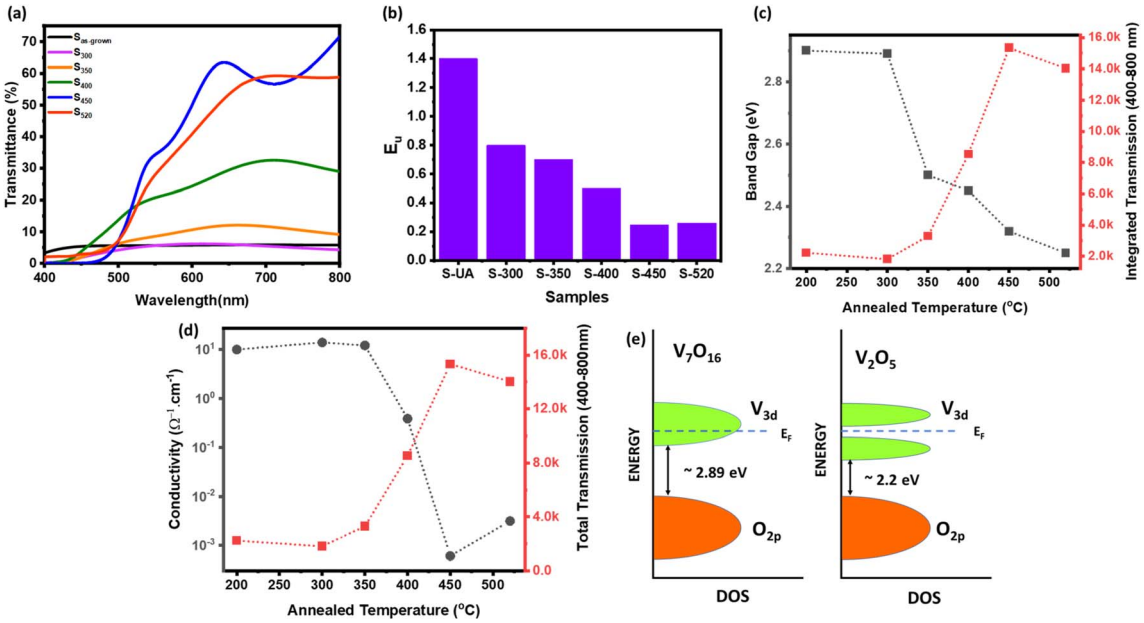


Fig. 3 (a) Optical transmission of vanadium oxide thin films annealed at different temperatures (b) Urbach energy of the samples (c) correlated with bandgaps and (d) conductivity of thin films (e) schematic band diagram of $V_2O_5$ and $V_7O_{16}$.

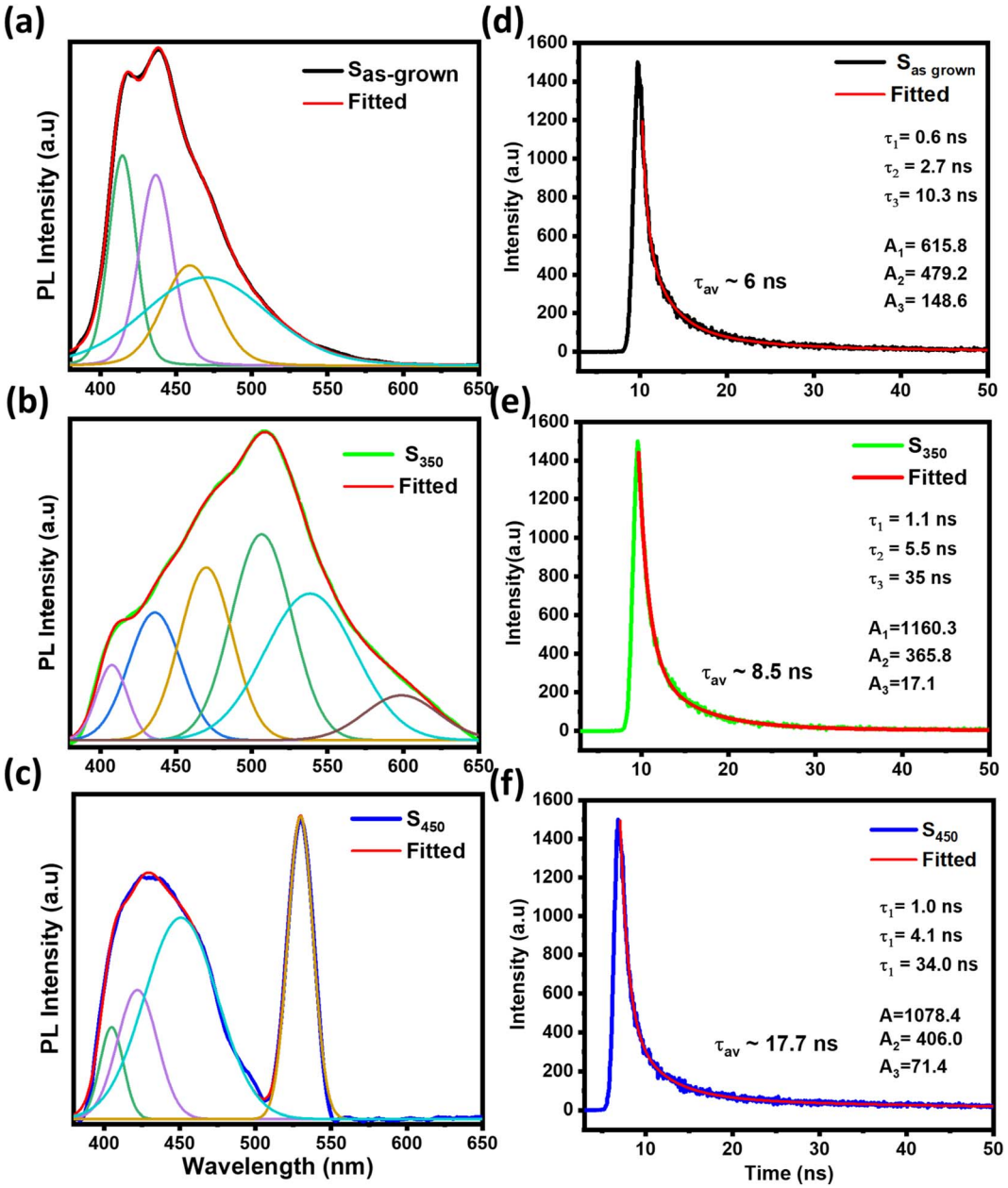


Fig. 4 (a–c) The photoluminescence (PL) and (d–f) time-resolved photoluminescence (TRPL) spectra of $S_{as\text{-}grown}$, $S_{350}$ and $S_{450}$ samples.

*versus* temperature measurements also confirms the metallic behavior of mixed phase, where the resistance is found to increase with temperature compared to pure $V_2O_5$ showing a typical decrease in resistance with temperature of semiconducting behavior, as shown in ESI Fig. S1.† The correlation of transmission with conductivity in Fig. 3(c) and (d) can be explained by reflection and absorption caused by higher metallicity and defect states, respectively.

The photoluminescence (PL) and time-resolved-photoluminescence (TRPL) results of $S_{as\text{-}grown}$, $S_{350}$, and $S_{450}$ are shown in Fig. 4. The peaks in PL spectra were deconvoluted using Gaussian function. The highest intensity peaks at ~438 nm, ~507 nm, ~530 nm can be assigned to the band-edge transitions from $V_{3d}$ conduction band to $O_{2p}$ valence band,[37] matching the bandgap value of each sample measured by UV-vis measurement in Fig. 3. The peaks at longer wavelengths in NIR can be assigned to the electronic transitions in mid-gap states

Table 2 Time-resolved photoluminescence (TRPL) parameters for the $S_{as\text{-}grown}$, $S_{350}$ and $S_{450}$ samples

| Sample | $A_1$ | $A_2$ | $A_3$ | $\tau_1$ (ns) | $\tau_2$ (ns) | $\tau_3$ (ns) | $\tau_{average}$ (ns) |
|---|---|---|---|---|---|---|---|
| $S_{as\text{-}grown}$ | 615.8 | 479.2 | 148.6 | 0.6 | 2.7 | 10.3 | 6.1 |
| $S_{350}$ | 1160.3 | 365.7 | 17.1 | 1.1 | 5.5 | 35.0 | 8.5 |
| $S_{450}$ | 1078.4 | 406.0 | 71.4 | 1.0 | 4.1 | 33.9 | 17.7 |

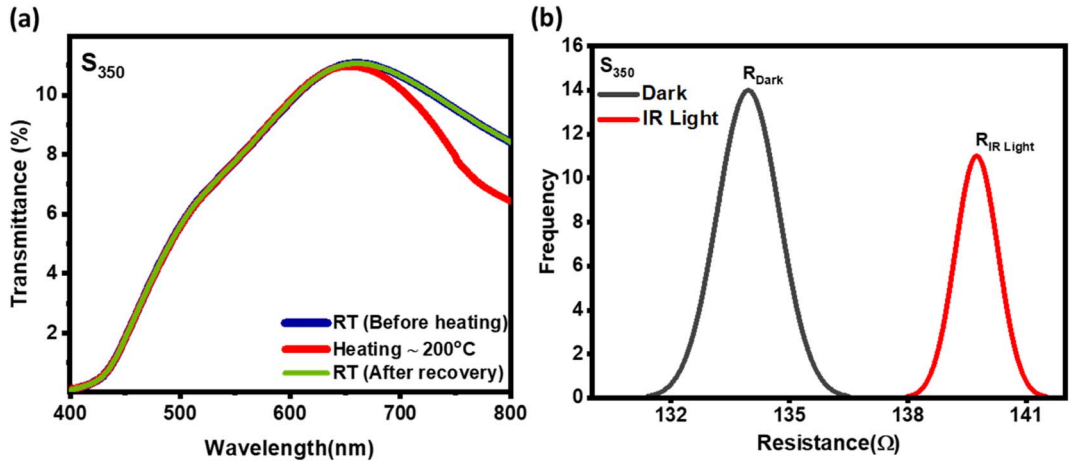


Fig. 5 (a) UV-spectra of the mixed phase before and after heating at 200 °C (b) the distribution of resistance value before and after illumination of under IR radiation.

due to oxygen vacancies, and the peaks at shorter wavelengths in UV are due to the transitions from higher $V_{3d}$ states to $O_{2p}$ bands.[37] Apparently, the more peaks in NIR are observed in amorphous and mixed phase samples due to large number of defects and oxygen vacancies compared to $V_2O_5$. The increased bandgap of mixed phase can be caused by the Burstein–Moss shift in PL spectra as a result of degenerate semiconducting behaviour of $V_7O_{16}$.[23,47]

To further investigate the nature of defects, we have measured the carrier life using TRPL as shown in Fig. 4(b) of $S_{as\text{-}grown}$, $S_{350}$, and $S_{450}$. In TRPL, the peak intensity decay ($I_{TRPL}$) with time ($t$) can be fitted using the following equation

$$I_{TRPL}(t) = \sum_{i}^{n} A_i e^{-t/\tau_i}$$

where $A_i$, $\tau_i$ are constants representing the amplitude and the lifetime of carriers. Here, we have used component $i = 3$ to fit the experimental curve and calculated the average decay time using the following expression

$$\tau_{av} = \frac{A_1\tau_1^2 + A_2\tau_2^2 + A_3\tau_3^2}{A_1\tau_1 + A_2\tau_2 + A_3\tau_3}$$

The extracted fitting parameters and average decay time are shown in Table 2. The decay constants $\tau_1$ and $\tau_2$ attributes to the fast decay through trap-mediated recombination, while $\tau_3$ corresponds to slow decay through radiative recombination.[37] The average decay time of $S_{450}$ is higher compared than other two samples due to the reduction in oxygen vacancies in the samples, which agrees well with the previous observations.[48] These results are in good agreement with the Urbach energy measurements shown in Fig. 3(b).

Finally, we demonstrate the sensitivity of our mixed phase sample by heating and IR radiation as shown in Fig. 5(a) and (b) respectively. Fig. 5(a) illustrate the optical transmission taken before and after heating the sample at 200 °C outside and then transferred to the UV-vis spectroscopy. Interestingly, a clear change in the transmission was only observed for the wavelengths higher than ~600 nm in near-IR (NIR) region. Indeed, no major change in the spectrum was observed in the visible range, indicating that these films are more sensitive to IR. Clearly, there will be some variations in temperature while taking the optical measurements, but the overall spectrum is always fully recovered as the samples is cooled back to the room temperature naturally.

Also, $V_7O_{16}$ being a degenerate semiconductor could also be suitable candidate for NIR plasmonics. Indeed, the broad peak ~650 nm in the UV-vis spectrum could be due to the NIR plasmons absorption.[23] Since the plasmonic frequency $\omega_p = \sqrt{ne^2/\varepsilon_0 m^*}$ is related to the carrier concentration ($n$) and the effective mass ($m^*$), where $e$ and $\varepsilon_0$ are electronic charge and the permittivity of free space, respectively. The measured value of resonant frequency ~$4.6 \times 10^{14}$ Hz gives the carrier concentration ~$10^{20}$ to $10^{21}$ cm$^{-3}$, which is also consistent with our conductivity values considering the theoretical values of mobilities and effective mass of vanadium oxides (1–1.7$m_e$).[49,50] The IR sensitivity in optical transmission is due to the plasmonic absorption and consistent with the earlier studied on the mixed phase of metallic $VO_2$ and insulating $V_2O_5$.[33] Also, the increase in resistance under IR radiation seen in Fig. 5(b) could be due to the electron–electron and electron–phonon scatterings as observed in metals and degenerate semiconductors in the resistance *versus* temperature measurements. Clearly, more low temperature transport measurements are required to further investigate the transport properties, but these results are encouraging for their promising use in smart-windows and IR sensors.

## Conclusions

In conclusion, we provide a detailed in-depth understanding of electronic and optical properties of $V_7O_{16}$ and systematically tune the electronic and optical properties of a mixed phase by changing the $V^{4+}$ and $V^{5+}$ contents. We report a strong modulation in the conductivity and optical transmission with infrared radiation and temperature. These results are very

promising for vanadium oxide based uncooled-IR sensors and smart windows that can be grown at low temperatures using a commercially viable cathodic vacuum arc-deposition technique.

## Conflicts of interest

There are no conflicts to declare.

## Acknowledgements

Anchal Rana acknowledges the research fellowship by BML Munjal University (BMU). Abhimanyu Rana would like to acknowledge SERB Core Research Grant CRG/2021/001136 and HMCL-BMU Research Grant BMU/RESOICSR/HMCL/2022/001 for the financial support. The authors at BMU would like thank Mr Piyush Chaturvedi and Mr Naresh Verma for their help during the experiments.

## References

1 A. Rogalski, *Infrared Phys. Technol.*, 2002, **43**, 187–210.
2 J. Wang, H. Fang, X. Wang, X. Chen, W. Lu and W. Hu, *Small*, 2017, **13**, 1–17.
3 A. Rogalski, *J. Appl. Phys.*, 2003, **93**, 4355–4391.
4 M. Strojnik, M. D'Acunto and A. Rogalski, *Appl. Opt.*, 2016, **55**, ITA1.
5 D. Benyahia, Ł. Kubiszyn, K. Michalczewski, A. Kębłowski, P. Martyniuk, J. Piotrowski and A. Rogalski, *Opt. Quantum Electron.*, 2016, **48**, 1–7.
6 K. Nakade, T. Kashiwagi, Y. Saiwai, H. Minami, T. Yamamoto, R. A. Klemm and K. Kadowaki, *Sci. Rep.*, 2016, **6**, 23178.
7 A. J. Kreisler and A. Gaugue, *Supercond. Sci. Technol.*, 2000, **13**, 1235.
8 F. J. Morin, *Phys. Rev. Lett.*, 1959, **3**, 34–36.
9 M. Imada, A. Fujimori and Y. Tokura, *Rev. Mod. Phys.*, 1998, **70**, 1039–1263.
10 C. Chen, X. Yi, J. Zhang and B. Xiong, *Int. J. Infrared Millimeter Waves*, 2001, **22**, 53–58.
11 Q. Cheng, T. Bui, M. Almasri and S. Paradis, *IEEE Sens. J.*, 2011, **11**, 167–175.
12 M. Nishikawa, T. Nakajima, T. Manabe, T. Okutani and T. Tsuchiya, *Mater. Lett.*, 2010, **64**, 1921–1924.
13 J. Jeong, N. Aetukuri, T. Graf, T. D. Schladt, M. G. Samant and S. S. P. Parkin, *Science*, 2013, **339**, 1402–1405.
14 P. Shvets, O. Dikaya, K. Maksimova and A. Goikhman, *J. Raman Spectrosc.*, 2019, **50**, 1226–1244.
15 M. Yuan, T. Huang, S. Wang, R. Zhang, Y. Yang, W. Yang, W. Wei, T. Zhang, W. Dong, X. Chen and N. Dai, *ACS Appl. Electron. Mater.*, 2019, **1**, 2308–2313.
16 J. Huotari, J. Lappalainen, J. Eriksson, R. Bjorklund, E. Heinonen, I. Miinalainen, J. Puustinen and A. Lloyd Spetz, *J. Alloys Compd.*, 2016, **675**, 433–440.
17 M. Roppolo, C. B. Jacobs, S. Upreti, N. A. Chernova and M. S. Whittingham, *J. Mater. Sci.*, 2008, **43**, 4742–4748.
18 R. T. Rajendra Kumar, B. Karunagaran, D. Mangalaraj, S. K. Narayandass, P. Manoravi, M. Joseph and V. Gopal, *Sens. Actuators, A*, 2003, **107**, 62–67.
19 M. M. Qazilbash, M. Brehm, B. G. Chae, P. C. Ho, G. O. Andreev, B. J. Kim, S. J. Yun, A. V. Balatsky, M. B. Maple, F. Keilmann, H. T. Kim and D. N. Basov, *Science*, 2007, **318**, 1750–1753.
20 V. R. Morrison, R. P. Chatelain, K. L. Tiwari, A. Hendaoui, A. Bruhacs, M. Chaker and B. J. Siwick, *Science*, 2014, **346**, 445–448.
21 P. T. P. Le, K. Hofhuis, A. Rana, M. Huijben, H. Hilgenkamp, G. A. J. H. M. Rijnders, J. E. ten Elshof, G. Koster, N. Gauquelin, G. Lumbeeck, C. Schüßler-Langeheine, H. Popescu, F. Fortuna, S. Smit, X. H. Verbeek, G. Araizi-Kanoutas, S. Mishra, I. Vaskivskyi, H. A. Dürr and M. S. Golden, *Adv. Funct. Mater.*, 2020, **30**, 1900028.
22 A. Rana, C. Li, G. Koster and H. Hilgenkamp, *Sci. Rep.*, 2020, **10**, 2–7.
23 Q. Wang, M. Brier, S. Joshi, A. Puntambekar and V. Chakrapani, *Phys. Rev. B*, 2016, **94**, 1–12.
24 S. Tepavcevic, H. Xiong, V. R. Stamenkovic, X. Zuo, M. Balasubramanian, V. B. Prakapenka, C. S. Johnson and T. Rajh, *ACS Nano*, 2012, **6**, 530–538.
25 Y. Wang, K. Takahashi, K. Lee and G. Cao, *Adv. Funct. Mater.*, 2006, **16**, 1133–1144.
26 R. Baddour-Hadjean, M. Safrany Renard, N. Emery, L. T. N. Huynh, M. L. P. Le and J. P. Pereira-Ramos, *Electrochim. Acta*, 2018, **270**, 129–137.
27 K. Schneider and W. Maziarz, *Sensors*, 2018, **2**, 2–6.
28 M. Yu, X. Liu, Y. Wang, Y. Zheng, J. Zhang, M. Li, W. Lan and Q. Su, *Appl. Surf. Sci.*, 2012, **258**, 9554–9558.
29 J. Huotari, J. Lappalainen, J. Puustinen and A. Lloyd Spetz, *Sens. Actuators, B*, 2013, **187**, 386–394.
30 T. K. Le, P. V. Pham, C. L. Dong, N. Bahlawane, D. Vernardou, I. Mjejri, A. Rougier and S. W. Kim, *J. Mater. Chem. C*, 2022, **10**, 4019–4071.
31 C. M. Lampert, *Mater. Today*, 2004, **7**, 28–35.
32 S. Kumar, A. Qadir, F. Maury and N. Bahlawane, *ACS Appl. Mater. Interfaces*, 2017, **9**, 21447–21456.
33 S. Y. Li, G. A. Niklasson and C. G. Granqvist, *Thin Solid Films*, 2012, **520**, 3823–3828.
34 J. Huotari, R. Bjorklund, J. Lappalainen and A. L. Spetz, *Procedia Eng.*, 2014, **87**, 1035–1038.
35 C. K. Christensen, E. D. Bøjesen, D. R. Sørensen, J. H. Kristensen, J. K. Mathiesen, B. B. Iversen and D. B. Ravnsbæk, *ACS Appl. Nano Mater.*, 2018, **1**, 5071–5082.
36 Z. Yang, C. Ko and S. Ramanathan, *Annu. Rev. Mater. Res.*, 2011, **41**, 337–367.
37 T. K. Le, M. Kang, S. W. Han and S. W. Kim, *RSC Adv.*, 2018, **8**, 41317–41322.
38 G. Silversmit, D. Depla, H. Poelman, G. B. Marin and R. De Gryse, *J. Electron Spectrosc. Relat. Phenom.*, 2004, **135**, 167–175.
39 A. Rana, A. Patra, M. Annamalai, A. Srivastava, S. Ghosh, K. Stoerzinger, Y.-L. Lee, S. Prakash, R. Y. Jueyuan, P. S. Goohpattader, N. Satyanarayana, K. Gopinadhan, M. M. Dykas, K. Poddar, S. Saha, T. Sarkar, B. Kumar,

C. S. Bhatia, L. Giordano, Y. Shao-Horn and T. Venkatesan, *Nanoscale*, 2016, **8**, 15597–15603.
40 J. Mendialdua, R. Casanova and Y. Barbaux, *J. Electron Spectrosc. Relat. Phenom.*, 1995, **71**, 249–261.
41 G. Silversmit, D. Depla, H. Poelman, G. B. Marin and R. De Gryse, *Surf. Sci.*, 2006, **600**, 3512–3517.
42 R. Baddour-Hadjean, M. B. Smirnov, V. Y. Kazimirov, K. S. Smirnov and J. P. Pereira-Ramos, *J. Raman Spectrosc.*, 2015, **46**, 406–412.
43 A. G. S. Filho, O. P. Ferreira, E. J. G. Santos, J. M. Filho and O. L. Alves, *Nano Lett.*, 2004, **4**, 2099–2104.
44 R. Baddour-Hadjean, M. B. Smirnov, K. S. Smirnov, V. Y. Kazimirov, J. M. Gallardo-Amores, U. Amador, M. E. Arroyo-de Dompablo and J. P. Pereira-Ramos, *Inorg. Chem.*, 2012, **51**, 3194–3201.
45 T. Blanquart, J. Niinistö, M. Gavagnin, V. Longo, M. Heikkilä, E. Puukilainen, V. R. Pallem, C. Dussarrat, M. Ritala and M. Leskelä, *RSC Adv.*, 2013, **3**, 1179–1185.
46 M. Kang, S. W. Kim, Y. Hwang, Y. Um and J. W. Ryu, *AIP Adv.*, 2013, **3**, 052129.
47 T. S. Moss, *Proc. Phys. Soc. B*, 1954, **67**, 775.
48 U. Özgür, A. Teke, C. Liu, S. J. Cho, H. Morkoç and H. O. Everitt, *Appl. Phys. Lett.*, 2004, **84**, 3223–3225.
49 A. S. Barker, H. W. Verleur and H. J. Guggenheim, *Phys. Rev. Lett.*, 1966, **17**, 1286–1289.
50 M. M. Qazilbash, M. Brehm, B.-G. Chae, P.-C. Ho, G. O. Andreev, B.-J. Kim, S. J. Yun, A. V. Balatsky, M. B. Maple, F. Keilmann, H.-T. Kim and D. N. Basov, *Science*, 2007, **318**, 1750–1753.